



ELSEVIER

Available online at www.sciencedirect.com

SCIENCE @ DIRECT®

Journal of Nuclear Materials 322 (2003) 21–35

Journal of
nuclear
materials

www.elsevier.com/locate/jnucmat

The influence of hydride blisters on the fracture of Zircaloy-4

O.N. Pierron^a, D.A. Koss^{a,*}, A.T. Motta^b, K.S. Chan^c

^a Department of Materials Science and Engineering, Pennsylvania State University, 202A Steidle Building, University Park, PA 16802, USA

^b Department of Mechanical and Nuclear Engineering, Pennsylvania State University, University Park, PA 16802, USA

^c Southwest Research Institute, San Antonio, TX, USA

Received 31 October 2002; accepted 29 May 2003

Abstract

The fracture behavior under near plane-strain deformation conditions of Zircaloy-4 sheet containing solid hydride blisters of various depths has been examined at 25 and 300 °C. The study was based on material with either model 'blisters' having diameters of 2 and 3 mm or a continuous layer of hydride; in all cases, the substrate material contained discrete hydride precipitates. The fracture strains decrease rapidly with increasing hydride blister/layer depth to levels of about 100 μm deep, and then remain roughly constant. For a given blister depth, the material is significantly more ductile at 300 °C than at room temperature although measurable ductility is retained even at 25 °C and for large blister depths. The material is somewhat more ductile if the hydride is in the form of a blister than in the form of a continuous layer (rim). The hydride blisters/layers are brittle at all temperatures, and crack shortly after yielding of the ductile substrate. Consequently, both experimental evidence and analytical modeling indicate that fracture of the sheet is controlled by the crack growth resistance of the substrate at 25 °C. At elevated temperatures, the hydride particles within the substrate are quite ductile, inhibit crack growth, and failure eventually occurs due to a shear instability.

© 2003 Elsevier B.V. All rights reserved.

1. Introduction

The mechanical behavior of Zircaloy fuel cladding degrades during nuclear reactor operation due to a combination of oxidation, hydriding, and radiation damage [1]. As the cladding undergoes oxidation with the associated hydrogen pickup, the total amount of hydrogen increases, and hydride precipitates form preferentially near the outer (cooler) surface of the cladding, usually in the form of a continuous layer/rim containing a high concentration of discrete hydrided particles. Under conditions where oxide spallation occurs, hydride blisters may form. The blisters are often lens shaped

(typically a few mm in major dimension) and consist of a very high hydride concentration or of a solid hydride [2].

The influence of a uniform distribution of hydrides on the mechanical behavior of zirconium-based alloys has been studied extensively, usually under uniaxial tensile loading; see for example Refs. [2–15]. Recent studies have also examined the failure behavior of Zircaloy-4 cladding tubes for the case when hydrides are present in the form of a layer or rim [14]. These 'hydride-rim' results, based on unirradiated cladding, indicate a significant loss of ductility with increasing hydrogen content and/or increasing hydride rim thicknesses and suggest that a ductile-to-brittle transition occurs with increasing hydride rim thickness.

In addition to the presence of hydrides, a second condition that affects cladding failure is the stress state associated with in-service loading. For the case of recrystallized (RX) zirconium alloy sheet containing a uniform distribution of hydrides, increasing the biaxiality of the stress state increases the severity of the

* Corresponding author. Tel.: +1-814 865 5447; fax: +1-814 865 2917.

E-mail address: koss@ems.psu.edu (D.A. Koss).

hydrogen embrittlement [15]. Such an effect becomes an issue for Zircaloy cladding subject to postulated reactor accidents such as the reactivity-initiated accident [16]. In this case, the interaction between fuel pellets and the cladding tubes forces the cladding to deform under multiaxial stress states. Predicting a criterion for cladding failure thus requires a knowledge of the influence of the effects of irradiation, the specific hydride microstructure, and the stress state of loading. This study addresses the latter two issues.

The purpose of this study is to examine the influence of *hydride blisters* on failure behavior of unirradiated Zircaloy-4 under the multiaxial stress state associated with near-plane strain deformation. To induce failure under a multiaxial stress state, we have designed a double-edge notched tensile specimen geometry that results in biaxial tension and near plane-strain tension deformation within the gauge section. In our case, the blisters exist as a solid hydride of varying depths with either a 2 or 3 mm diameter; as a benchmark, a few results are also presented for the case of a continuous layer of a solid hydride. Finally, in order to avoid the difficulty of preparing, testing, and analyzing the behavior of very small ring-stretch specimens derived from cladding tubes, we utilize flat Zircaloy-4 sheet with a crystallographic texture (and plastic anisotropy) similar to that of as-fabricated Zircaloy-4 cladding tubes. Both cold worked and stress-relieved (CWSR) as well as RX conditions of the sheet are examined.

2. Experimental procedure

2.1. Materials used

Zircaloy-4 sheet with a thickness of 0.64 mm was obtained from Teledyne Wah-Chang in the CWSR. RX material was obtained after annealing the as-received material at 650 °C for 30 min in a vacuum of 10^{-5} Torr. The grain structure, determined using polarized light microscopy, consisted of elongated grains, approximately 10 μm long and roughly 1–2 μm thick in the CWSR condition and of equiaxed grains approximately 5 μm grain in diameter in the RX condition.

Both the CWSR and RX conditions exhibited a strong crystallographic texture. The Kearns factors (resolved fraction of basal poles aligned with the three macroscopic directions, N = normal, L = longitudinal (rolling direction), T = transverse) [17], measured by Teledyne Wah-Chang are shown in Table 1. The majority of the basal poles are aligned with the normal direction. Importantly, these values are similar to those reported for unirradiated CWSR Zircaloy-4 cladding tubes [18] if the hoop direction of the tube corresponds to the orientation transverse to the rolling direction of the sheet. Therefore, the texture of the sheets of Zirca-

Table 1
Kearns factors for both CWSR and RX Zircaloy-4 sheet and tubing

	f_N	f_L	f_T
CWSR sheet (this work)	0.59	0.05	0.31
RX sheet (this work)	0.60	0.06	0.34
CWSR tubing [17]	0.58	0.10	0.32

loy-4 used in this study is similar to the typical texture of Zircaloy-4 cladding tubes, for which the basal planes tend to align with their poles inclined approximately $\pm 30^\circ$ away from the normal of the tube surface and oriented towards the transverse direction [19].

The tensile properties of the Zircaloy-4 sheet used in this study are shown in Table 2 and are described in more detail elsewhere [20]. The RX condition exhibits a much higher strain hardening exponent ($n = d \ln \sigma / d \ln \epsilon$, where σ is the stress and ϵ is the strain) but lower yield stress values than the CWSR condition. Also yield stress at 300 °C is much lower than that at 25 °C, as is the case for Zircaloy-4 cladding tube [21]. In both conditions, the texture observed above causes the Zircaloy-4 sheet to be plastically anisotropic such that through-thickness deformation is difficult. Such behavior is apparent from the values of the plastic anisotropy parameter R' ($R' = \epsilon_{\text{width}} / \epsilon_{\text{thickness}}$, where ϵ_{width} and $\epsilon_{\text{thickness}}$ are the width and thickness strains during uniform deformation in a tensile test); for the conditions listed in Table 2, R' is in the range of 1.6–5.2.

It is instructive to compare the tensile behavior of our CWSR sheet tested in the transverse direction with that of CWSR Zircaloy-4 cladding tubing as tested in the hoop direction of the tube. The yield strength of the cladding is somewhat higher at room temperature (≈ 120 MPa) and at 300 °C (≈ 100 MPa) [21]. Both materials have similar plastic anisotropy values, but the strain-hardening exponent of the sheet used in this study ($n = 0.01$ – 0.03) is significantly smaller than that of standard cladding ($n \approx 0.06$) [22]. In fact, the strain hardening behavior of this sheet material is similar to that of irradiated cladding [23].

Table 2
Tensile parameters of Zircaloy-4 sheet in either the RX or CWSR conditions at 25 and 300 °C for uniaxial testing in the transverse direction of the sheet

Condition	$\sigma_y^{0.2\%}$ (MPa)	n -value	R'	Elongation to failure (%)
RX/25 °C	469	0.09	5.2	29
CWSR/25 °C	573	0.01	2.2	19
RX/300 °C	166	0.11	2.2	29
CWSR/300 °C	318	0.03	1.6	16

2.2. Hydrogen charging

Hydrogen charging of the Zircaloy-4 was performed by gas charging at 400 °C using a Ni ‘window’ whose geometry controlled the dimensions of the hydride layer (i.e., blister or continuous layer). Shown schematically in Fig. 1(a), the Ni window consisted of a thin film of Ni ($\approx 0.1 \mu\text{m}$ thick) that was vapor deposited onto the specimen gauge section with the following geometries: (a) a 2 mm circle, (b) a 3 mm circle (for most of this study), and (c) a continuous layer. A short time period prior to vapor deposition, the surface of Zircaloy was cleaned using the ASTM procedure (G2-88) to remove the small oxide layer that is normally present in Zr exposed to atmosphere. Uncoated regions of the Zircaloy quickly reformed the small oxide layer prior to exposure to the hydrogen/argon gas at the 400 °C, inhibiting the diffusion of hydrogen and restricting the hydride formation to regions below/near to the Ni coating. As described in detail elsewhere [24], hydrogen charging was performed at 400 °C by exposing the coated specimen to a gas mixture of 12.5% H_2 /Argon at one atmosphere pressure and for charging times ranging from 30 s to 30 min. For a given material, it was observed that the depth of the blister was a linear function of the charging time. For the range of charging times used, cross-section metallography showed that the blister diameter corresponded to the Ni coating diameter. In addition, some hydrogen diffused throughout the sheet thickness to form discrete hydrides in the ‘substrate’ region beneath the hydride blister. The hydrogen concentration within the substrate was measured by hot vacuum fusion analysis. The resulting hydride distribution is illustrated schematically in Fig. 1(b) with l being the blister width (2 or 3 mm) and d the blister depth.

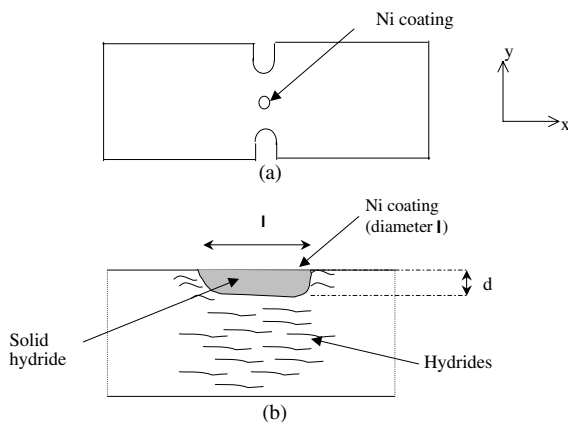


Fig. 1. A schematic of (a) a double edge notched tensile specimen with a Ni coating/hydride blister in its center and (b) hydride blister made by hydrogen charging through a Ni coating with diameter l .

The hydride microstructure after charging was examined using both light microscopy and scanning electron microscopy (SEM). Specimens were prepared for examination by mechanical grinding ranging from 240 to 1200 grit and polishing to a 6 μm finish using a diamond solution. The specimens were then etched up to 5 s with a 10 part HNO_3 –10 part H_2 –1 part HF solution to reveal the hydrides.

2.3. Mechanical testing

In-service loading of Zircaloy cladding tubes usually occurs under multiaxial tension with the maximum principal stress oriented in the hoop direction of the tube. Based on earlier studies [22], we have simulated such loading with a double edge notched tensile specimen, Fig. 1(a), designed to introduce a biaxial stress state in the specimen center such that near plane-strain tension is achieved (i.e., the minor strain component in the plane of the sheet is near zero). After an experimental design process, 25.4 mm wide specimens (≈ 76 mm long) with two 4.75 mm diameter notches, each of which was 6.35 mm deep, were selected. The resulting biaxial state of stress in the center of the specimen limits strain in the transverse direction of the specimen and induces the material near its center to a near plane-strain deformation path. While sharper notches increase the biaxiality of the stress state, the notch also acts as a strain concentrator. Thus, very sharp notches elevated the local strain to a level that fracture initiated near the notch, rather than in the specimen center where near plane-strain deformation is occurring. For the specimen geometry selected (with the 4.75 mm diameter notch) failure occurred in the specimen center, where a near plane-strain condition is met, and where the hydride blister was located.

The mechanical testing was performed at an approximate strain rate of 10^{-3} s^{-1} . Most of the tests were performed at either room temperature or 300 °C, but limited tests were also done at 400 °C. In addition, the orientation of the tensile axis was chosen to be in the long transverse direction of the sheet (normal to the rolling direction) in order to obtain deformation behavior similar to that of unirradiated Zircaloy-4 cladding when tested in the hoop direction.

As will be shown later, the hydride blisters fractured at, or shortly after, yielding within the ductile substrate. Acoustic emission as well as interrupted testing was used to detect the formation of the microcracks within the hydride blisters. Failure strains of the substrate material beneath the blister were determined by measuring the local fracture strain $(\epsilon_{\text{frac}})_{\text{local}}$ near, but not at, the fracture surface. After measurement of the initial specimen thickness, cross-section metallography of the fractured specimen was used to determine the specimen thickness at a location ≥ 0.5 mm displaced from the fracture

surface. For sheet of 0.6 mm thickness containing small cracks, distances of 0.5 mm or greater from the fracture surface avoided a localized thickness reduction due to the plasticity associated with either crack growth (room temperature failure) or a localized shear instability (300 °C failure); thus, as is common in studies of the failure of sheet metal [24,25], the strain values determined in this manner indicate the strain level at the onset of failure. Using this procedure, we calculated a local thickness strain, ε_3 , that indicates the strain level at the onset of failure. This thickness strain value was then converted into a local failure strain $(\varepsilon_{\text{frac}})_{\text{local}}$ value using the ratio of minor $(\varepsilon_2)_{\text{blister}}$ and major $(\varepsilon_1)_{\text{blister}}$ strains within the substrate beneath the blister (measured from the deformation of the circular Ni coating which subsequently deforms into an ellipse during testing) and using conservation of the volume. Thus,

$$(\varepsilon_{\text{frac}})_{\text{local}} = \frac{-\varepsilon_3}{1 + \frac{(\varepsilon_2)_{\text{blister}}}{(\varepsilon_1)_{\text{blister}}}}. \quad (1)$$

No spallation of the Ni coating was ever detected even at large strains indicating adherence to the substrate. For the case in which specimens were hydrided across the entire gauge length (a hydride rim), a microhardness indentation gridding procedure was used to determine the ratio $\varepsilon_2/\varepsilon_1$ on a local basis as done previously [22].

3. Results and discussion

3.1. Hydride microstructure

As a result of the hydrogen charging procedure, the blisters were defined by the formation of a solid hydride to a near-uniform depth beneath the Ni coating, as is shown in Fig. 2. In the present study, blisters with primarily a 3 mm diameter were formed with depths ranging from 5 to 250 μm .

In addition to the formation of a solid hydride blister, some of the hydrogen also forms individual hydride precipitates in the substrate below the hydride blister. As

shown in Fig. 2(a), these hydride precipitates typically have a major dimension on the scale of 100 μm in the CWSR condition and, except for a thin layer immediately below the blister, the hydrides tend to be aligned in the plane of the sheet, similar to the circumferential hydride microstructures in Zircaloy cladding tube. In contrast, the hydrides within the substrate in the RX material appear somewhat smaller ($\approx 25 \mu\text{m}$ maximum dimension) and tend to be more random in orientation, especially close to the hydride blister (see Fig. 2(b)). After removing by mechanical grinding the hydride blister, the hydrogen concentrations in the ligament below the blister were measured as a function of blister thickness for both RX and CWSR conditions. Results from six different conditions (hydride depths ranging from 50 to 175 μm) show that the H content within the ligament increases from approximately 300 wt. ppm for the 50 μm blister depth to approximately 400 wt. ppm within the substrate below blisters with depths $>100 \mu\text{m}$. Thus, while the general characteristics of the hydride microstructure within the substrate differed between the CWSR and RX materials, both hydrogen analyses and metallography indicate that blister depth had only a minor effect on the substrate microstructure for a given condition.

In summary, the resulting microstructure consists of a combination of a hydrided substrate residing beneath a solid hydride blister whose width corresponds to the Ni coating dimension (typically 3 mm diameter) and whose depth is controlled by the charging time at 400 °C. To some extent, the hydride microstructure would be affected by the time at the 300 °C test temperature; to minimize this effect, we uniformly limited the test time at 300 °C to roughly 10 min followed by air cooling. It is useful to compare the microstructure shown in Fig. 2(a) (the CWSR case) to that formed during in-reactor operation of Zircaloy-4 cladding. Fig. 3, taken from a Zircaloy-4 cladding tube irradiated to 67 GWd/t, shows a solid hydride layer with a depth $\sim 50 \mu\text{m}$ as well as the presence of a concentration of discrete, circumferential hydride precipitates. A comparison of Figs. 2 and 3 shows that the morphology (shape, aspect ratio, orien-

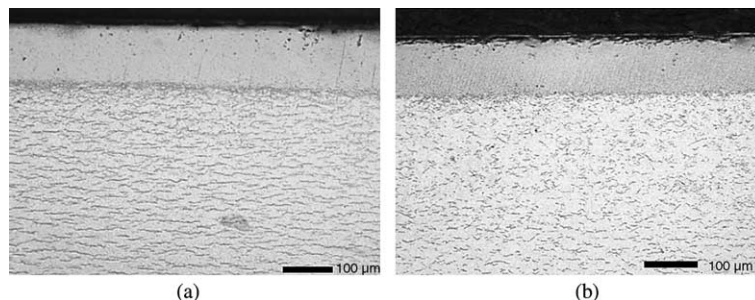


Fig. 2. Light micrographs of a transverse section of Zircaloy-4 sheet showing hydride blister and discrete hydride precipitates within the substrate beneath the blister in (a) CWSR specimen and (b) RX specimen.

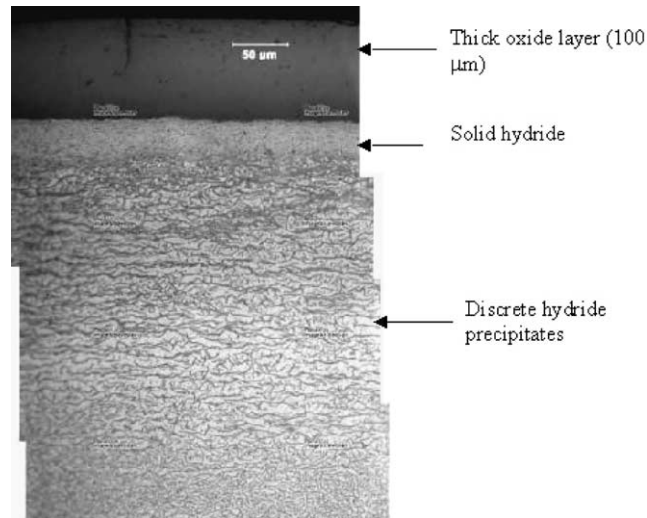


Fig. 3. A light micrograph showing a hydride layer and associated hydrides in the substrate beneath the layer in irradiated Zircaloy-4 cladding tube (average fuel burnup of 67 GWd/t and fast fluence of 1.3×10^{22} n/cm²). (Courtesy of R. Daum, Argonne National Laboratory.)

tation) of the hydrides in the substrate under the model blisters in this study is similar to that observed in the material hydrided in service.

3.2. Effect of blister depth on sheet failure

Previous research has shown that the thickness of a continuous hydride rim has a strong influence on the failure of Zircaloy-4 cladding; specifically, increasing the thickness of the hydride rim decreases the ductility of the cladding [14,27]. A similar effect is observed for the case of hydride blisters. The presence of the brittle blister causes the initiation of a crack that propagates to the depth of the blister, as described in more detail in the

sections below. Failure of the sheet is then controlled by fracture of the ductile substrate beneath the blister, which fails at various strain levels, depending on the depth of the blister.

Fig. 4 shows that the local fracture strain of the Zircaloy-4 sheet containing 3 mm blisters initially decreases rapidly with increasing hydride blister depth for both material conditions and at 300 °C as well as 25 °C. The rapid decrease in failure strain with increasing blister depth persists to about 100 μm depth. Moderate ductility (7–10% fracture strain for the cold worked material and 10–15% for RX condition) is retained at 300 °C, even for blisters of depths > 200 μm. In contrast, at 25 °C the retained ductility is only 3–5%. Fig. 4 also

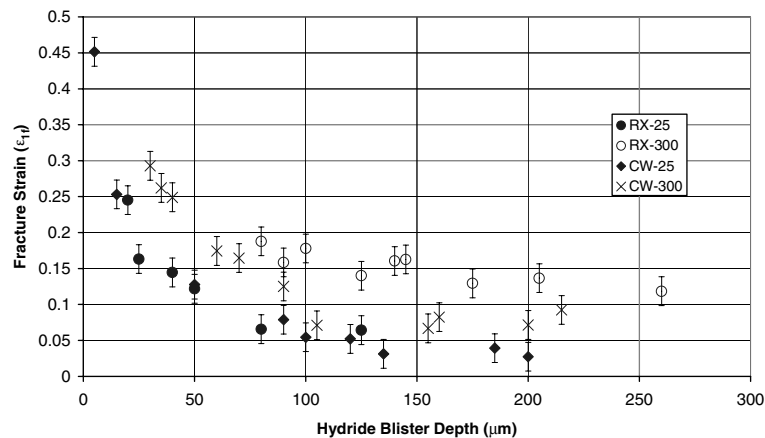


Fig. 4. Local fracture strain versus hydride blister thickness for both CWSR and RX Zircaloy-4 sheet tested at either 25 or 300 °C. All data are for 3 mm blisters.

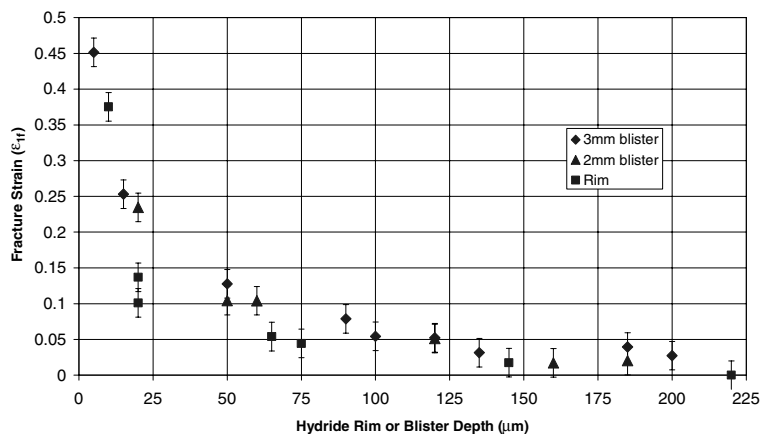


Fig. 5. Local fracture strain versus blister or rim depth for either 3 or 2 mm diameter hydride blisters or a continuous rim of hydrides (25 °C).

shows that, for a given blister depth, the material is significantly more ductile at 300 °C than at 25 °C. Although both the CWSR and the RX conditions show similar behavior at 25 °C, the RX condition shows significantly more ductility at a given blister depth at 300 °C. This result is somewhat surprising since the RX condition contains a higher fraction of radial hydrides (known to promote fracture) within the substrate.

Fig. 5 compares the variation of the local fracture strain at 25 °C with blister depth for two blister sizes (2 or 3 mm). It is clear that the two curves match and thus at least at 25 °C, the ductility of specimens with hydride blisters depends mainly on the depth of the blister rather than on its diameter.

Fig. 5 also compares the influence of blisters on fracture with that of a continuous hydride rim. Although both the blister and rim cases, the ductility decreases rapidly with increasing hydride layer depth up to depths of ~100 μm, the decrease in fracture strain is more severe when the hydride layer is present in the form of a rim, especially at small blister/rim depths. For example, the fracture strain for a specimen with a 3-mm diameter and a 20 μm thick blister is ≈0.24, while it is only ≈0.12 for a specimen with a 20 μm continuous hydride rim. Similar results, although not as complete as those in Fig. 5, have been obtained for specimens tested at 300 °C; in that case all three tests performed on specimens with hydride rims depths of less than 60 μm showed the Zircaloy with a rim to have less ductility than the Zircaloy with blisters [26]. Thus, the ductility of a material containing a continuous hydride rim is less than that of a material containing blisters of the same depth.

Comparing to previous studies performed on tubing [14,27], the fracture strains obtained in this study with *sheet material* containing a hydride rim are very similar to those obtained previously on *tubing* with hydride rim.

The similarity in fracture strain values lends support to our contention that the behavior of sheet material is a good model for that of tubing material with similar texture and hydride microstructure.

Finally, we call attention to the fact that, along with increased fracture strain at small blister depths, there is also a change in strain path. For thick blisters, the lateral constraint from the blister and the presence of cracks forces the Zircaloy substrate to a condition close to plane-strain deformation (i.e., referring to Fig. 1, $\varepsilon_{yy} \approx 0$). Alternatively, the lack of transverse constraint from thin blisters as well as the high R -value of the substrate sheet metal results in a significantly larger minor strain in specimens with thin blisters. This change in strain path likely contributes to the observed increase fracture strain (Figs. 4 and 5). We offer this speculation on the basis that fracture of sheet metal usually depends on a critical thickness strain criterion [28]. Thus, any change in strain path in which the minor strain increases requires a compensating increase in major strain to achieve the critical thickness strain. In short, sheet metal ductility usually increases as the strain path deviates from plane-strain tension.

3.3. Mode of failure: fracture profiles

While failure of the Zircaloy sheet initiates with cracking of the blisters at both 25 and 300 °C, the mode of fracture of the substrate material (which determines the ductility of the hydrided sheet) depends on temperature. Fig. 6 shows that the fracture profiles differ significantly between specimens tested at 25 and 300 °C. Independent of blister depth, the fracture profiles at 25 °C are characterized by crack growth along a path roughly *normal to specimen surface* and therefore also normal to the maximum principal stress. Given the presence of 300–400 wt. ppm hydrogen in the substrate

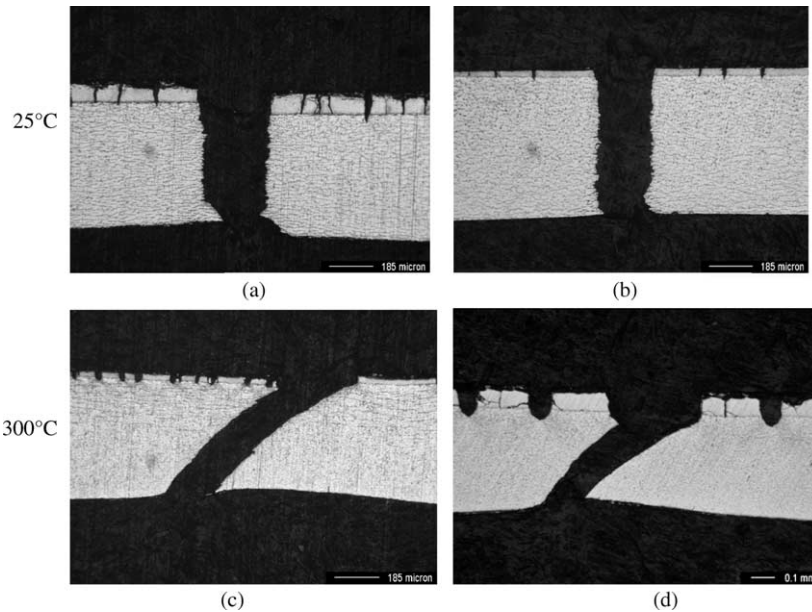


Fig. 6. Fracture profiles of (a) CWSR sheet with a 100 μm blister, (b) RX with 40 μm blister, (c) CWSR with 35 μm blister, and (d) RX with 80 μm blister. Test temperatures are indicated.

which results in hydride precipitates, crack growth appears to result from damage accumulation within the substrate in the form of voids initiated by cracked hydrides, as shown in Fig. 7. Thus, at 25 °C, failure of the Zircaloy substrate occurs as a result of a crack growth process on a plane normal to the maximum principal stress and involving the growth and coalescence of voids formed by the cracked hydride precipitates.

In contrast to behavior at room temperature, fracture of the substrate at 300 °C substrate failure occurs on a macroscopic plane inclined at $\approx 45^\circ$ through the thickness, as also shown in Fig. 6(c) and (d). Such behavior suggests an alternate failure mode to crack growth. Specifically, the through-thickness shear failure evident in Fig. 6(c) and (d) strongly suggests a deformation lo-

calization process in which deformation localizes on a plane of high shear stress, as in the manner of localized necking of sheet metal [28,29]. The pronounced crack blunting at 300 °C indicates that cracks initiating within the blister are arrested by a very ductile, crack-resistant substrate. The cracks appear to be significantly more blunted in the RX condition than in the CWSR condition. This behavior is consistent with the increased ductility of the RX condition (see Fig. 4).

3.4. Fracture of hydride blisters

The failure behavior of Zircaloy sheet with hydride blisters (and, we believe, Zircaloy cladding tubes with hydride blisters) can be understood as a sequential

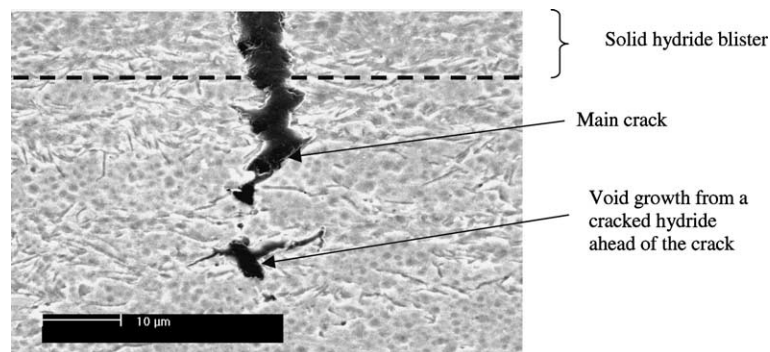


Fig. 7. A light micrograph showing fractured hydrides and void nucleation near the tip of a crack beneath a 200 μm blister in CWSR Zircaloy-4 deformed at room temperature.

process of crack initiation within the hydride blister and the subsequent failure of the substrate material beneath the blister. Consistent with previous observations of hydride blister fracture at room temperature and 200 °C [30], interrupted testing shows that the blisters crack at small plastic strains ($\epsilon_1 \leq 0.02$) within the substrate beneath the blister. This is supported by acoustic emission measurements. Fig. 8 shows the results of acoustic emission measurements performed at room temperature in material containing a 3 mm diameter, 30 μm deep model blister. The experiment recorded 28 intense acoustic emission ‘hits’ (shown inside the oval) occurring at/or shortly after yielding; these hits correspond to the 28 cracks present. Nearly all cracks propagated to the full blister depth and width. Furthermore, measurements of the blister geometry and crack opening displacements also indicate that $\epsilon_1 < 0.02$ beneath uncracked segments of the blister. Similarly, tests interrupted at small strains ($\epsilon_1 \leq 0.02$) also show a population of cracks within the blisters at 300 °C and even at 400 °C.

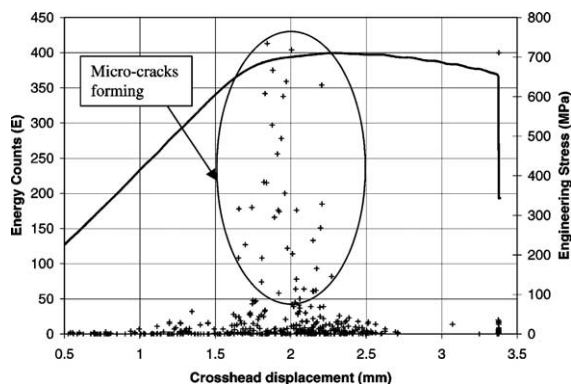


Fig. 8. The occurrence of acoustic emission events (represented by their energy counts) during a mechanical test at 25 °C of a CWSR specimen containing a blister 30 μm deep.

Similar to room temperature observations, measurements of strains within the blisters themselves indicate $\epsilon_1 \leq 0.015$. In all cases, cross-section metallography shows the cracks are oriented normal to the blister surface and extend through its depth, consistent with their brittle behavior; the cracks arrest at the ductile substrate. Thus, we conclude that the hydride blisters are brittle at temperatures ≤ 400 °C.

Because the blisters are not only brittle but also reside on a ductile substrate, multiple cracks (all of which extend the width of the blister) form during deformation of the sheet, as illustrated in Fig. 9. An examination of cracked blisters, such as those in Fig. 9, suggests that the cracks within the blister have a fairly regular spacing, and that the crack spacing increases with blister depth. As depicted in Fig. 10, detailed measurements of the spacing between adjacent cracks in fact show that the spacing between cracks that form at room temperature in thick blisters (≥ 50 μm) is roughly equal to the blister depth (solid line in Fig. 10). At 300 °C, the data suggest somewhat larger crack spacing (between 1 and 1.5 t) (small dashed line), see Fig. 10. In contrast, for thin blisters (< 50 μm) Fig. 10 indicates they follow an approximate relationship of $y = 1.4 t$ (large dashed line). As a result, only a few, comparatively deep, cracks form within thick blisters, while a high density of short cracks form within thinner blisters. In contrast, for thin blisters (≤ 50 μm), Fig. 10 suggests significantly larger spacing between cracks for specimens tested at room temperature. Finally, we note that at 300 °C, the data suggest somewhat larger crack spacing than at room temperature for the thick blister case. In all cases, the crack that eventually propagates and causes failure is usually spaced a distance about 2–3 crack depths from its neighboring crack.

The cracking behavior shown in Figs. 9 and 10 can be readily understood using a straightforward shear lag analysis, such as is employed in predicting the fragmentation of embedded fibers in a ductile matrix composite [31,32]. As the Zircaloy substrate deforms, it

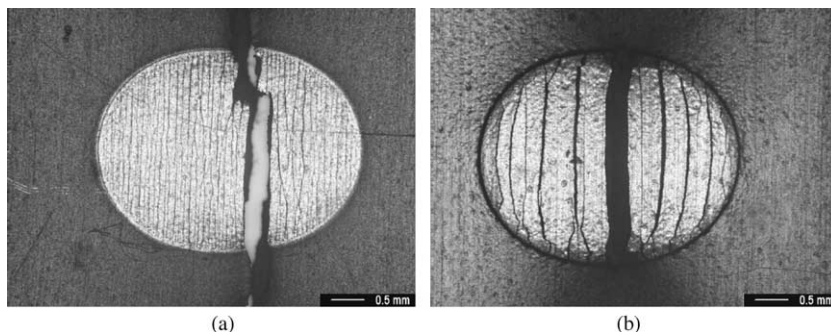


Fig. 9. Macrographs of cracked blisters in CWSR material failed at (a) 25 °C and with a 50 μm deep blister and (b) 300 °C with a 105 μm deep blister.

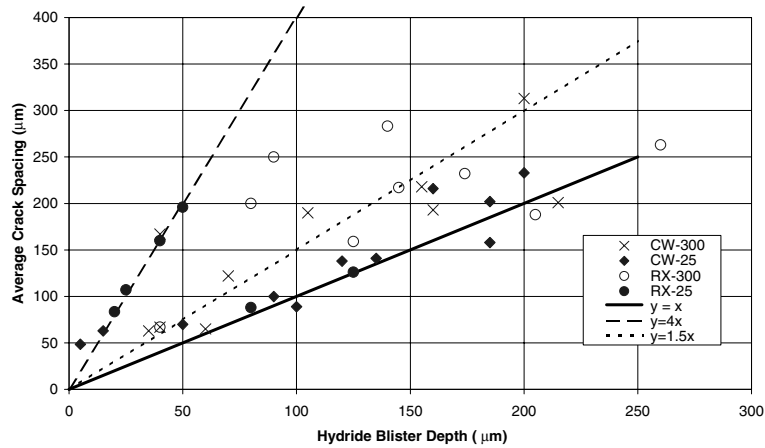


Fig. 10. Crack spacing within the hydride blisters versus blister depth for the four test conditions.

transfers load to the blister on a scale dictated by the shear stress, τ , at the blister–substrate interface. For a blister of width, W , the force balance dictates a stress on the blister, (σ_B) , that is related to the force exerted by the substrate with a shear strength τ by the following relationship:

$$\tau\lambda W = (\sigma_B)tW, \tag{2}$$

where λ is the spacing between cracks, t is the hydride thickness.

In addition to the stress, σ_B , applied to the blister by the deforming substrate, the hydride blister will likely contain residual compressive stresses, σ_{res} , owing to (a) the $\approx 14\%$ volume expansion accompanying the formation of the hydride and (b) the difference in thermal expansion coefficients between the hydride blister and Zircaloy substrate (also causing compressive stresses in the blister on cooling from 400 °C to the test temperature). Thus, the hydride blister fracture stress, $(\sigma_B)_f$, is simply the sum of the applied and residual stress as given by

$$(\sigma_B)_f = \tau(\lambda/t) + \sigma_{res}. \tag{3}$$

Fig. 10 indicates that the average crack spacing λ and hydride blister thickness t are related, and those data suggest specific dependences of crack spacing on blister thickness that are a function of blister depth and tem-

perature; these λ – t relationships are listed in Table 3. To predict the fracture stress of the blister, we need to know the shear strength of the substrate and an estimate of the residual stress in the hydride. For our plane-stress condition, the shear strength is $\tau = (1/2)\sigma_1$, where σ_1 is the maximum principal stress. Given the yield stress of the Zircaloy-4 sheet in Table 2, assuming the hydride precipitates in the matrix do not significantly affect the yield stress, and taking into account the plastic anisotropy (Table 2), we can calculate the τ -value for the substrate–blister shear stress. In doing so, we assume plane-strain deformation of the substrate for thick blisters (where their presence constrains the minor strain, ε_2 , to a near zero value, $\varepsilon_2/\varepsilon_1 \cong 0$), but a strain-path between plane-strain tension and uniaxial tension for the case of thin blisters. In the thin-blister case, for RX sheet at 25 °C, $\varepsilon_2/\varepsilon_1 \cong -0.5$, while for CWSR sheet, $\varepsilon_2/\varepsilon_1 \cong -0.4$; given the yield stresses and plastic anisotropies, we obtain $\sigma_1 \cong 685$ MPa for both cases, using the early Hill analysis [33].

In order to estimate the magnitude of the residual stresses, σ_{res} , in Eq. (3), we assume that the residual stress caused by the transformation to the hydride phase is limited by the flow stress of the matrix at 400 °C. Based on the 300 °C flow stresses in Table 1, we estimate the compressive component of σ_{res} to be ≈ -150 MPa and ≈ -280 MPa for the RX and CWSR materials, respectively. An additional residual compressive stress

Table 3
The predicted values for the fracture stresses of hydride blisters for three different conditions

Condition	λ – t relationship	Blister fracture stress $(\sigma_B)_f$ (MPa)
Thin blister ($\leq 50 \mu\text{m}$) at 25 °C RX substrate	$\lambda \approx 4.0t$	≈ 1050
Thick blisters ($\geq 50 \mu\text{m}$) at 25 °C RX and CWSR substrates	$\lambda \approx (1.0\text{--}1.2)t$	≤ 100
Thick blisters at 300 °C	$\lambda \approx (1.4\text{--}2.1)t$	≤ 70

develops in the blister on cooling from the 400 °C charging temperature to the test temperature, and we estimate this component as $E_{ZrH}(\alpha_{ZrH} - \alpha_{Zr})(400 - T)$. This component creates an additional compressive residual stress of ≈ -160 MPa at room temperature and -40 MPa at 300 °C. For example, combining these two residual stress components for the case of the RX material, we estimate a residual compressive stress of -310 MPa.

Based on the behavior shown in Fig. 10 and the analysis above, Eq. (3) may be used to estimate the hydride blister fracture stress. As shown in Table 3, thin hydride blisters (≤ 50 μm) appear to have a significantly higher fracture stress (~ 1050 MPa, based on Eq. (3)) than the thick blisters (≤ 100 MPa), most likely due to the decreased probability of the presence of a flaw. Using bend testing, Leger et al. also observe that the thicker blisters crack at lower applied stresses; for air-jet-grown blisters on Zircaloy-2 pressure tubes, hydride blisters of depths ≈ 35 μm failed at stresses of ≈ 700 MPa [30], which is somewhat lower than the 1050 MPa value estimated in Table 3 for our blisters in the range of 20–50 μm . Leger et al. also predict a negligible fracture stress for blisters greater than 100 μm [30], which is consistent with the small fracture stresses estimated for our thick blisters, most of which are greater than 100 μm thick (see Fig. 10). That larger hydrides are more likely to fracture is evident from the data of Kuroda et al. [10], who report a very low fracture stress of 18 MPa for bulk tensile specimens of $\text{ZrH}_{1.73}$. Such a value is more than an order of magnitude lower than the fracture stress deduced from our data.

3.5. Fracture of hydride precipitate particles

Previous studies have observed that finite plastic strains within the matrix are required to fracture hydride precipitate particles and to form voids in Zr–2.5Nb and Zircaloy [5–9,13]. This behavior is consistent with detailed experimental observations that indicate that hydride particles can undergo significant plastic deformation before cracking [7,13]. In the present study, the smallest strain to fracture hydrides ('hydride fracture strain') was obtained by examining the cross-sections of fracture specimens using SEM at 1000 \times to locate cracked hydrides *and* the associated void at positions farthest from the fracture surface (i.e., at the smallest strain). Care was taken in etching the specimen not only to remove any smeared metal that might cover a cracked hydride but also to maintain edge retention at voids and minimize chemical attack of the hydrides; Fig. 7 is an example of the image quality.

In order to determine the hydride fracture strain, the thickness of the specimen at the location of a cracked hydride particle was measured and the associated thickness strain was then transformed into an equivalent

plastic strain assuming Hill's original yield function under plane-strain conditions [33]:

$$\bar{\epsilon} = \sqrt{\frac{2}{3}} \sqrt{\frac{(2+R')(1+R')}{1+2R'}} \sqrt{\epsilon_1^2 + \frac{2R'}{1+R'} \epsilon_1 \epsilon_2 + \epsilon_2^2}, \quad (4)$$

where ϵ_1 and ϵ_2 are calculated knowing the thickness strain and their ratio ϵ_2/ϵ_1 (determined by blister dimensions at fracture). Our hydride fracture strain thus corresponds to an equivalent strain necessary to nucleate a void density of 80 voids/ mm^2 , which corresponds to one cracked hydride in an area 120×100 μm^2 , as viewed in the SEM at 1000 \times . It should be recognized that at this location, many uncracked hydrides were present and that the so-called hydride fracture strain is a minimum value of the matrix strain to fracture hydride precipitate particles.

As shown in Fig. 11, there is a finite hydride fracture/void nucleation strain, ϵ_{void} , associated with cracked hydride particles. Specifically, $\epsilon_{\text{void}} \cong 0.10$ for both CWSR and RX materials at 25 °C. While significant in magnitude, this ϵ_{void} -value is somewhat less than that (~ 0.20) reported in earlier studies examining hydride fracture in Zircaloy-4 [14]. As in previous studies [7,13], there is a marked effect of temperature on ϵ_{void} such that in this study at 300 °C the hydrides do not crack until $\epsilon_{\text{void}} \cong 0.16$ for the cold-worked condition and a much greater value, $\epsilon_{\text{void}} \cong 0.28$, in the RX state. Thus, the hydride precipitates require more strain to fracture at 300 °C than at 25 °C, especially in RX Zircaloy-4. The increased ductility of hydride precipitates at elevated temperatures was used to explain the decreased sensitivity of Zircaloy-4 to hydrogen embrittlement at 350 °C by Bai et al. [7], and our results may also be interpreted to indicate an increased ductility within the hydrides at 300 °C.

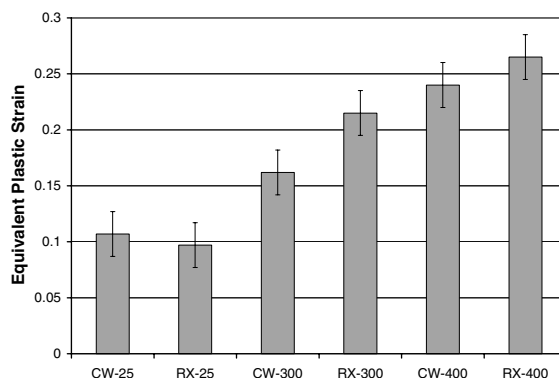


Fig. 11. Equivalent plastic strain to initiate fracture within hydride particles in both CWSR and RX conditions of Zircaloy-4 tested at 25, 300, and 400 °C.

4. Fracture mechanics analysis for room temperature failure

The results described above indicate that the fracture behavior is sensitive to blister depth as well as temperature. In all cases, the hydride blisters crack at small strains and fracture of the sheet is controlled by failure of the ductile substrate beneath the blister. While substrate failure at 300 °C appears to result from a shear instability, room temperature fracture has the characteristics of crack growth (i.e., fracture along a plane normal to σ_1 accompanied by comparatively little local necking). In this section we present an elastic–plastic analysis to predict fracture strains for fracture at room temperature. A previous fracture mechanics analysis addressed crack growth from a hydride rim in Zircaloy on the basis of a fracture *stress* [34,35]. Unfortunately, in most of our experiments failure occurs near the tensile strength and the previous analysis does not capture the strong sensitivity of fracture *strain* to blister depth. We develop here a fracture mechanics approach to predict the fracture *strain* necessary to propagate the crack within blister of given depth.

As an initial basis for the analysis, we assume that the hydride blister/rim of depth a is equivalent to a single crack of the same initial depth (the important issue of parallel cracks and shielding is discussed below). The geometries for both hydride rim and blister configurations correspond to a semi-infinite surface crack or a semi-elliptical surface crack, respectively. In both cases, the cracks reside in a sheet of finite thickness, and we assume plane-stress conditions through the thickness. Because of the large amount of plastic yielding that occurs during crack growth, elastic–plastic fracture mechanics based on the J -integral approach is used. The J -integral approach is particularly suitable for treating crack growth in a thin sheet since it allows large-scale plasticity at the crack tip. Nakamura and Parks have shown that the J -integral remains a valid parameter for characterizing the crack driving force in a fully plastic thin sheet even when the crack-tip plastic zone exceeds the thickness of the sheet [36]. For the notched thin sheet problem considered here, the principal stress in the thickness direction (σ_3) is zero; thus, the plane stress condition is satisfied. In addition, the presence of the notch in the thin sheet creates a biaxial stress state with $\sigma_1 > \sigma_2 > 0$ such that the plastic strain (ε_2^p) in the width direction is almost zero. When the elastic strains are small compared to the plastic strains and can be ignored, a plane-strain condition exists in the plane since $\varepsilon_1^p = -\varepsilon_3^p$ with $\varepsilon_2^p = 0$. In applying the J -integral approach to this problem, the elastic–plastic crack in this thin sheet is considered to be driven primarily by the maximum principal stress, σ_1 (the lateral stress (σ_2) is ignored since it is aligned parallel to the crack). An isotropic elastic–plastic fracture theory is used here as an

approximation because the corresponding J -integral theory for anisotropic materials has yet to be developed. It is also uncertain that an anisotropic theory would give significantly better results. Details of the J -integral fracture analysis is described below.

In order to account for isotropic plasticity, the material is assumed to follow the Ramberg–Osgood equation:

$$\frac{\varepsilon}{\varepsilon_0} = \frac{\sigma}{\sigma_0} + \alpha \left(\frac{\sigma}{\sigma_0} \right)^{n'}, \quad (5)$$

where σ_0 is the yield stress, $\varepsilon_0 = \sigma_0/E$, n' is the inverse of the strain-hardening exponent ($n' = 1/n$), and $\alpha = \sigma_0^{n'-1} E/k^{n'}$ with k defined by the relationship $\sigma = k\varepsilon^n$. Therefore, the plastic strain at the crack tip is equal to

$$\varepsilon_n^p = \alpha \frac{\sigma_0}{E} \left(\frac{\sigma_n}{\sigma_0} \right)^{n'}, \quad (6)$$

where σ_n is the net-section stress, $\sigma_n = \sigma/(1 - (a/t))$.

Fracture occurs when the driving force for the crack propagation, $J(a_e, \sigma)$, reaches the critical value J_c ; and so the condition for crack propagation can be expressed as

$$J(a_e, \sigma) = J_c = \frac{K_c^2}{E}, \quad (7)$$

where K_c is the plane-stress fracture toughness of the sheet. The J -integral may be separated into elastic $J_e(a_e, \sigma)$ and plastic $J_p(a_e, \sigma)$ components:

$$\begin{aligned} J(a_e, \sigma) &= J_e(a_e, \sigma) + J_p(a_e, \sigma) \\ &= J_e(a_e, \sigma) \left[1 + \alpha \left(\frac{\sigma_n}{\sigma_0} \right)^{n'-1} \right], \end{aligned} \quad (8)$$

where $J_e(a_e, \sigma) = K_c^2/E$ for plane-stress conditions. Substituting (6) into Eq. (5) leads to the following relationship for the fracture plastic strain:

$$\varepsilon_n^p = \alpha \frac{\sigma_0}{E} \left\{ \frac{1}{\alpha} \left(\frac{K_c^2}{K_c^2} - 1 \right) \right\}^{n'/(n'-1)}. \quad (9)$$

Eq. (9) permits us to predict the fracture strain provided that we know the stress-intensity factor K_e for the crack geometries. In all cases, we apply the ‘plastic zone correction’ procedure by considering a hypothetical crack of length $a_e = a + r_{0\sigma}$, where $r_{0\sigma}$ is half of the plastic zone size in plane-stress conditions or

$$r_{0\sigma} = \frac{1}{2\pi} \left(\frac{K_e}{\sigma_0} \right)^2. \quad (10)$$

The plastic zone $2r_{0\sigma}$ is obtained by first calculating K_e with $a_e = a$; then K_e is recalculated using $a_e = a + r_{0\sigma}$.

In order to determine the stress intensity parameter for the case of the cracked hydride blisters, the crack geometry correction factor for a semi-elliptical crack in a strip of finite thickness was employed [37]. For the case of the continuous hydride rim, the correction factor was that for a semi-infinite surface crack in a strip of finite thickness. These correction factors are based on the presence of a single crack in the material. However, the experimental results, Figs. 6 and 9, show the presence of multiple parallel cracks along the blister or the rim. Based on the results of Isida et al. for a parallel array of equally spaced equal semi-elliptical surface cracks, considerable crack-tip shielding is expected *if* the cracks are of equal depth [38]. Incorporating the shielding analysis by Isida et al. into the fracture model, however, resulted in an over-prediction of the fracture strains, unless an unrealistically low K_c -value was used for the Zircaloy-4.

To resolve the above discrepancy, the microcrack shielding formulation by Rose [39] was used to compute the interactions between a pair of symmetrically disposed microcracks and a main crack. The analysis is based on the presence of microcracks with lengths $2s$ that are located at a radial distance R and an angular position, θ , measured from the tip of the main crack to the center of the microcracks. The configuration of the microcracks and the main crack is shown in Fig. 12(a), which also presents the result of the shielding ratio, K_{tip}/K , where K_{tip} is the local stress intensity factor at the tip of the main crack, and K is the far-field stress intensity factor of the applied load. A shielding ratio greater than unity indicates microcrack anti-shielding, while $K_{tip}/K < 1$ indicates microcrack shielding. The computed values of K_{tip}/K , shown in Fig. 12(a), indicate microcrack shielding exists only when $150^\circ > \theta > 70^\circ$, which was also reported by Rose [39]. The location where the maximum shielding effect occurs is at $\theta \cong 100\text{--}110^\circ$. In our fracture mechanics analysis, the crack tip is located at the plastic zone. As a result, the

microcracks are located at an angle, $\theta \approx 150^\circ$ measured from the tip of the main crack, Fig. 12(b). For this crack configuration, the microcracks exert little shielding on the main crack. If the main crack and the microcracks start out at equal depths, the main crack would experience some shielding effect from the microcracks. However, the effect would diminish as the main crack extended and propagated away from the microcracks. Eventually the shielding effect would be completely gone when the tip of the main crack reached the plastic zone boundary shown in Fig. 12(b). In either case, the shielding effect should be negligible, and our analysis is based on the development of a single dominant crack.

In order to apply the crack-growth analysis described, the fracture toughness, K_c , must be known. For Zircaloy-4 cladding tubes, previous studies show K_c -values depend on H content and temperature. K_c -values in the range of $120\text{--}150 \text{ MPa m}^{1/2}$ are common for unhydrided Zircaloy-4 at both room temperature and 300°C . At room temperature, Grigoriev et al. [40] found K_c -values about $104 \text{ MPa m}^{1/2}$ for H contents $400\text{--}600 \text{ wt. ppm}$ (assuming the following relationship: $K_c = \sqrt{J_{\max} E}$, with J_{\max} the J_I -integral for the maximum load point, and E the elastic modulus). Based on data from Huang [41], Kuroda et al. assumed K_{IC} -values of $73 \text{ MPa m}^{1/2}$ in their fracture mechanics analysis of hydrided Zircaloy-4 cladding at room temperature [34]. At 300°C , the H content does not appear to influence the fracture toughness [40], in which case $K_c \cong 120\text{--}150 \text{ MPa m}^{1/2}$ [1]; Grigoriev et al. report a J_{\max} -value that indicates $K_c \cong 117 \text{ MPa m}^{1/2}$ at 300°C for 400 wt. ppm H [40]. The nominal stress σ was calculated using Hill's original yield function for plane-strain condition and the constitutive stress-strain relation expressed in Eq. (5) with the equivalent strain being given by Eq. (4). An iterative calculation was then made to obtain the fracture strain ε_n^p . The material properties used in the analysis for both temperatures and materials (CWSR and RX) are given in Table 4.

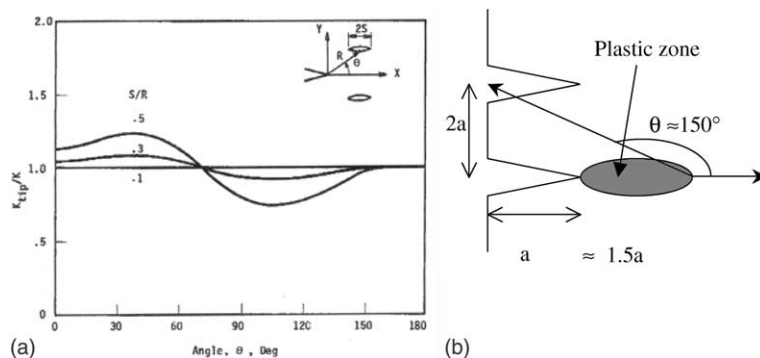


Fig. 12. (a) Crack tip stress intensity factor for the main crack as a function of the location of two parallel cracks whose angular location is determined by the angle θ and (b) the geometry of neighboring cracks in the present study.

Table 4
Material properties used in the fracture mechanics analysis

Property	CWSR		RX	
	25 °C	300 °C	25 °C	300 °C
n	0.01	0.025	0.087	0.112
n'	100	40	11.5	8.9
E (GPa)	100	75	100	75
σ_0 (MPa)	573	318	469	166

Fig. 13 shows the comparison between the fracture mechanics predictions and the observed dependences of fracture strain on blister/rim depth. As shown in Fig. 13(a), at room temperature the agreement between experimental results and crack growth predictions are quite good assuming $K_c = 70 \text{ MPa m}^{1/2}$, which is close to the value of $73 \text{ MPa m}^{1/2}$ assumed by Kuroda et al. [34]. Bearing in mind that our substrate material contains 300–400 wt. ppm hydrogen, the 70 MPa -value is similar but somewhat less than that ($90 \text{ MPa m}^{1/2}$) observed by Grigoriev et al. [40]. Close inspection of Fig. 13(a) shows that both the predictions and the observed fracture strains for the two blister diameters (2 and 3 mm) are superimposed on each other. This behavior supports our earlier conclusion that the blister diameter (2 or 3 mm) has no significant effect on the failure of Zircaloy-4.

Agreement similar to that shown in Fig. 13(a) is also obtained between prediction of our crack growth analysis and the observed influence of the continuous hydride rim on fracture, also on the basis of $K_c \cong 70 \text{ MPa m}^{1/2}$. The predicted fracture mechanics results also confirm the earlier experimental observation that, compared to a hydride blister, a continuous hydride rim is somewhat more deleterious to ductility at a given hydride depth.

For the case of the RX materials, at 25 °C the crack growth analysis fits experimental observations, using a K_c -value between 100 and $150 \text{ MPa m}^{1/2}$. While somewhat surprising, the increased K_c -value of the RX material is consistent with its lower flow stress and increased tensile ductility. For example, an unhydrided plane strain specimen was tested as well as a sister sample hydrided in the form of discrete hydride precipitates through the whole thickness below the Ni coating (no solid hydride blister was present) at a H concentration similar to that of the hydrided substrates, both at room temperature and in the RX condition. Very similar average strains were found. Those results show that the tensile ductility of the hydrided substrate is similar to that of the unhydrided material and, importantly, significantly higher in the RX compared to the CWSR condition. Thus, it is reasonable the RX material exhibits more crack growth resistance than the CWSR material.

5. On predicting failure at 300 °C

At 300 °C, Fig. 13(b) shows that fracture mechanics no longer predicts the observed dependence of fracture strain on hydride blister depth. This lack of agreement is consistent with our earlier experimental observations, Fig. 6, that indicate a transition in failure mode occurs from crack growth at room temperature to shear instability at 300 °C. Such transition is likely a result of the fact that the strains to nucleate voids at cracked hydride particles increase markedly with increasing temperature (Fig. 11). It is also consistent with the observation of a much reduced level of hydrogen embrittlement in Zircaloy-4 at 350 °C [7]. Thus, we expect a significant increase in fracture strain within the crack-tip process zone and therefore higher fracture toughness at 300 °C,

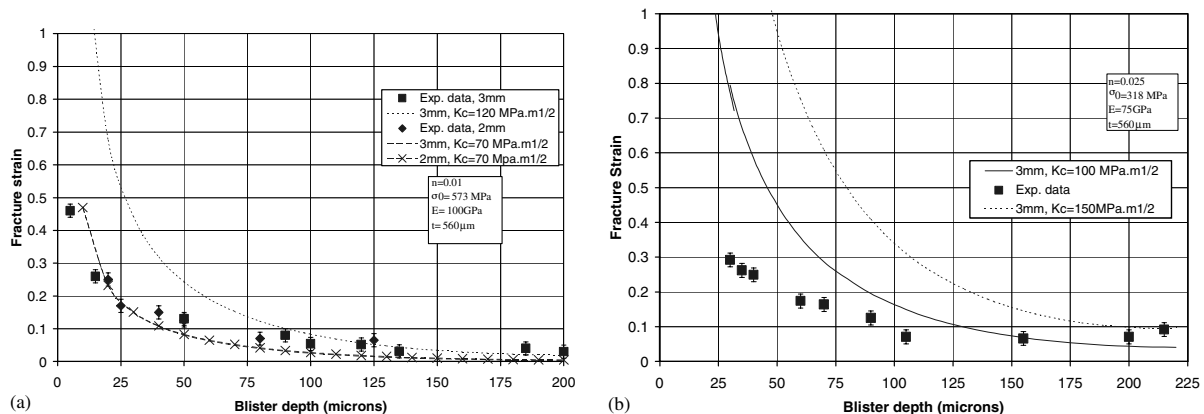


Fig. 13. The dependence of observed and predicted fracture strains for CWSR Zircaloy-4 with hydride blisters at (a) 25 °C and (b) 300 °C.

consistent with experimental observations [39]. At 300 °C; application of the analysis in Section 4, results in a significant over-prediction of the experimentally observed fracture strains as a consequence of the elevated values of the fracture toughness. Thus, upon testing of Zircaloy-4 at high temperatures we see that Zircaloy-4 containing hydride blisters does not fail by crack growth, but rather by a competing mechanism, i.e. a deformation localization process in which failure occurs by shear localization. Thus, an alternate failure model should be used to predict the experimental data at 300 °C.

6. Conclusions

Both CWSR and RX Zircaloy-4 sheet specimens were hydrided to form either 2 or 3 mm solid hydride blisters of controlled depths residing on a substrate that contain ~300–400 wt.ppm hydrogen in the form of discrete hydride particles. Limited tests were also performed on material with a continuous hydride layer. The fracture behavior of these materials were studied (primarily at 25 and 300 °C) using double edge notched tensile specimens designed to induce near plane-strain deformation. The main conclusions are as follows:

1. The hydride blisters are brittle in all test temperatures examined, from 25 to 400 °C. A population of cracks forms and propagates through the blisters soon after the yielding of the plastic substrate beneath the hydride blister. A straight-forward analysis of the crack spacing within the blisters indicates a blister fracture stress that depends on blister depth with thin blisters ($\leq 50 \mu\text{m}$) having a significantly higher fracture stress.
2. Fracture of the sheet was controlled by the crack growth resistance of the substrate: the fracture strains decreased with increasing hydride blister/layer depth to levels of about 100 μm deep, above which the ductility remained constant. At 300 °C, both the CWSR and RX Zircaloy-4 retained moderate ductility (7–10% fracture strain for CWSR and 10–15% for the RX condition), even for blister depths $>200 \mu\text{m}$, which is close to one-third of the sheet thickness.
3. For a given blister depth, the material is significantly more ductile at 300 °C than at room temperature. Also, the sheet is somewhat more ductile if the hydride is present as a blister rather than as a continuous layer. Blisters with 2 or 3 mm diameter have the same effect on sheet ductility.
4. An examination of the fracture profiles indicates a transition in failure mode within the substrate from crack growth on a plane normal to the maximum principal stress at 25 °C to a shear instability process on an inclined plane at 300 and 400 °C. At room temperature, the cracks that initiate within the hydride

blisters (as well as in the continuous layers) propagate in a manner that can be predicted using elastic-plastic fracture mechanics. The observed fracture strains and their dependence on hydride blister depth can be predicted using a reasonable value of the fracture toughness.

5. The hydride precipitate particles within the substrate are ductile, and exhibit a fracture strain that increases with increasing temperature. The resulting increase in void nucleation strain contributes to an elevation of the fracture toughness at high temperatures to a level that causes the observed transition to failure due to a shear instability process within the substrate (as opposed to crack growth).

Acknowledgements

We would like to thank Dave Green and Rob Daum at Penn State for many technical discussions and Ralph Meyer at the NRC for his continued encouragement. This research has been supported by the Fermi Consortium at Penn State (ONP) and by the Southwest Research Institute (KSC).

References

- [1] C. Lemaignan, A.T. Motta, in: B.R.T. Frost (Ed.), Nuclear Materials, vol. 10B, VCH, New York, 1994, p. 1.
- [2] A.M. Garde, G.P. Smith, R.C. Pirek, in: 11th International Symposium on Zr in the Nuclear Industry, vol. STP 1295, ASTM, Garmisch-Partenkirchen, 1996, p. 407.
- [3] C.E. Coleman, D. Hardie, *J. Less-Common Met.* 2 (1966) 168.
- [4] C.E. Ells, *J. Nucl. Mater.* 28 (1968) 129.
- [5] L.A. Simpson, *Metall. Trans. A* 12A (1981) 2113.
- [6] T.M. Link, D.A. Koss, A.T. Motta, *Metall. Mater. Trans.* 31A (2000) 1883.
- [7] J.B. Bai, C. Prioul, D. Francois, *Metall. Mater. Trans. A* 25A (1994) 1185.
- [8] F. Prat, M. Grange, J. Besson, E. Andrieu, *Metall. Mater. Trans. A* 29A (1998) 1643.
- [9] M. Grange, J. Besson, E. Andrieu, *Metall. Mater. Trans. A* 31A (2000) 679.
- [10] M. Kuroda, K. Yoshioka, S. Yamanaka, H. Anada, F. Nagase, H. Uetsuka, *J. Nucl. Sci. Tech.* 37 (2000) 670.
- [11] M. Kuroda, S. Yamanaka, D. Setoyama, M. Uno, K. Takeda, H. Anada, F. Nagase, H. Uetsuka, *J. Alloys Compd.* 330–332 (2002) 404.
- [12] S.I. Hong, K.W. Lee, K.T. Kim, *J. Nucl. Mater.* 303 (2002) 169.
- [13] S. Arsene, J.B. Bai, P. Bombard, *Metall. Mater. Trans. A* 34A (2003) 553, and 579.
- [14] R.S. Daum, S. Majumdar, M.C. Billone, D.W. Bates, D.A. Koss, A.T. Motta, in: 13th ASTM International Symposium on Zr in the Nuclear Industry, ASTM STP 1423, Annecy, France, 2001, p. 702.
- [15] F. Yunchang, D.A. Koss, *Metall. Trans. A* 16A (1985) 675.

- [16] R.O. Meyer, R.K. McCardell, H.M. Chung, D.J. Diamond, H.H. Scott, Nucl. Safety 37 (1996) 372.
- [17] J.J. Kearns, C.R. Woods, J. Nucl. Mater. 20 (1966) 241.
- [18] P. Delobelle, P. Robinet, P. Bouffieux, P. Greyer, I. LePichon, in: 11th International Symposium on Zr in the Nuclear Industry, ASTM STP 1295, Garmisch-Partenkirchen, 1996, p. 373.
- [19] E. Tenckhoff, deformation mechanisms, texture and anisotropy in zirconium and zirconium alloys, vol. 966, ASTM, Philadelphia, 1988.
- [20] O.N. Pierron, D.A. Koss, A.T. Motta, J. Nucl. Mater. 312 (2003) 257.
- [21] T.M. Link, Failure of Zircaloy cladding under severe loading conditions, M.Sc. thesis, in: Materials, Penn State University, University Park, PA, 1997.
- [22] T.M. Link, D.A. Koss, A.T. Motta, Nucl. Eng. Des. 186 (1998) 379.
- [23] SCDAP/RELAP5/MOD2, Code Manual volume 4: MATPRO: A Library of Materials Properties for Light Water Reactors Accident Analysis, NUREG/CR-5273, EG-2555, 1990, Chapter 4.9.
- [24] S.S. Hecker, Sheet Metal Ind. 52 (1975) 671.
- [25] S.S. Hecker, Formability: Analysis, Modeling, and Experimentation, TMS, 1978, p. 150.
- [26] O. Pierron, M.S. thesis, The Pennsylvania State University, 2002.
- [27] R.S. Daum, S. Majumdar, H. Tsai, T.S. Bray, D.A. Koss, A.T. Motta, M.C. Billone, in: Proceedings of the 4th International Symposium on Small Specimen Test Techniques, ASTM STP 1418, 2002, 195.
- [28] K.S. Chan, D.A. Koss, A.K. Ghosh, Metall. Trans. A 15A (1984) 323.
- [29] Z. Marciniak, J. Duncan, Mechanics of Sheet Metal Forming, E. Arnold, London, 1992.
- [30] M. Leger, G.D. Moan, A.C. Wallace, N.J. Watson, in 8th International Symposium: Zirconium in the Nuclear Industry, ASTM STP 1023, San Diego, 1989, p. 50.
- [31] H.L. Cox, Br. J. Appl. Phys. 3 (1952) 73.
- [32] A. Kelly, Strong Solids, Oxford, 1973.
- [33] R. Hill, The Mathematical Theory of Plasticity, Oxford University, 1950.
- [34] M. Kuroda, S. Yamanaka, F. Nagase, H. Uetsuka, Nucl. Eng. Des. 203 (2001) 185.
- [35] S. Yamanaka, M. Kuroda, D. Setoyama, M. Uno, K. Takeda, F. Nagase, H. Uetsuka, J. Alloys Compd. 330–332 (2002) 400.
- [36] T. Nakamura, D.M. Parks, in: A.J. Rosakis, K. Ravichandar, Y. Rajapakse (Eds.), AMD, vol. 91, ASME, NY, 1988, p. 227.
- [37] N.E. Dowling, Mechanical Behavior of Materials: Engineering Methods for Deformation, Fracture, and Fatigue, Prentice Hall, 1999.
- [38] M. Isida, T. Yoshida, H. Noguchi, Eng. Fract. Mech. 39 (1991) 845.
- [39] L.R.F. Rose, Int. J. Fract. 31 (1986) 233.
- [40] V. Grigoriev, B. Josefsson, B. Rosborg, in: 11th International Symposium on Zr in the Nuclear Industry, ASTM STP 1295, Garmisch-Partenkirchen, Germany, 1996, p. 431.
- [41] F.H. Huang, J. Nucl. Mater. 207 (1993) 103.